Harmonic Viscoelastic Response of 3D Histology-Informed White Matter Model

Xuehai Wu¹, John G. Georgiadis, ², and Assimina A. Pelegri¹*

¹Department of Mechanical and Aerospace Engineering, Rutgers, the State University of New Jersey, 98 Brett Road, Piscataway, NJ 08854-8058, USA

*E-mail: pelegri@rutgers.edu

² Department of Biomedical Engineering, Illinois Institute of Technology, 3255 S. Dearborn St., Wishnick Hall 314, Chicago, IL 60616, USA

Keywords:

Myelinated Axons Homogenization Viscoelastic properties Finite elements simulation Magnetic Resonance Elastography

ABSTRACT

White matter (WM) consists of bundles of long axons embedded in a glial matrix, which lead to anisotropic mechanical properties of brain tissue, and this complicates direct numerical simulations of WM viscoelastic response. The detailed axonal geometry contains scales that range from axonal diameter (microscale) to many diameters (mesoscale) imposing an additional challenge to numerical simulations. Here we describe the development of a 3D homogenization model for the central nervous system (CNS) that accounts for the anisotropy introduced by the axon/neuroglia composite, the axonal trace curvature, and the tissue dynamic response in the frequency domain. Homogenized models that allow the incorporation of all the above factors are important for accurately simulating the tissue's mechanical behavior, and this in turn is essential in interpreting non-invasive elastography measurements.

Geometric and material parameters affect the material properties and thus the response of the brain tissue. More complex, orthotropic, or anisotropic material properties are to be considered as necessitated by the 3D tissue structure. An assembly of micro-scale 3D representative elemental volumes (REVs) is constructed, leading to an integrated mesoscale WM finite element model. Assemblies of microscopic REVs, with orientations based on geometrical reconstructions driven by confocal microscopy data are employed to form the elements of the WM model. Each REV carries local material properties based on a finite element model of biphasic (axon-glial matrix) unidirectional composite. The viscoelastic response of the microscopic REVs is extracted based on geometric information and fiber volume fractions calculated from the relative distance between the local elements and global axonal trace. The response of the WM tissue model is homogenized by averaging the shear moduli over the total volume (thus deriving effective properties) under realistic external loading conditions. Under harmonic shear loading, it is proven that that the effective transverse shear moduli are higher than the axial moduli when the axon moduli are higher than the glial. Methodologically, the process of using micro-scale 3D REVs to describe more complex axon geometries avoids the partition process in traditional composite finite element methods (based on partition of finite element grids) and constitutes a robust algorithm to automatically build a WM model based on available axonal trace information. Analytically, the model provides unmatched simulation flexibility and computational power as the position, orientation, and the magnitude of each tissue building block is calculated using real tissue data, as are the training and testing processes at each level of the multiscale WM tissue.

1. INTRODUCTION

White matter (WM) constitutes approximately 50% of the brain and 60-80% of the spinal cord in humans, and its integrity is highly significant in health or disease (Fern, 2017; Saab and Nave, 2017). The explosive growth in mechanobiology knowledge indicates that WM mechanics on the cell level is an important regulator of the development or repair of the central nervous system (Franze et al., 2013). Consistent with findings across various pathologies in all biological tissues (Holle et al., 2017), it has been suggested that changes in mechanical properties of WM as a result of normal aging, injury, or disease are not only a consequence of local tissue structure changes but essential biomarkers for the progression of brain aging (Lamoureux et al., 2010) or disease (Pogoda and Janmey, 2018; Urbanski et al., 2019). In parallel, there has been a growing emphasis on non-invasive techniques to assess WM mechanics in vivo. One such promising modality is Magnetic Resonance Elastography (MRE) (Murphy et al., 2019), which produces full-field maps of effective mechanical properties of WM by interpreting the propagation of harmonic shear waves in the tissue. The MRE methodology involves the extraction of shear strain fields from displacement data, followed by the computational solution of an inverse problem to estimate the local viscoelastic properties of the tissue. Owing to intrinsic MRI limitations, MRE introduces several constraints for the mechanical characterization of brain tissue relative to ex vivo methods. MRE is based on detecting the shear waves generated by external mechanical actuation of the skull that generates low ($\sim 10^{-4}$) shear harmonic strain. In contrast, ex vivo methods involve medium to finite-strain of ostensibly homogeneous specimens under quasistatic, creep/relaxation, constant strain tensile/compression, oscillatory shear, indentation, or impulsive actuation of brain or spine tissues (Chatelin et al., 2010) (Koser et al., 2015). The large scatter of brain viscoelastic properties reported is consistent with findings implying that the WM is mechanically heterogeneous (Johnson et al., 2013a), anisotropic (Anderson et al., 2016), and its effective properties depend strongly on the loading conditions, as well as on test conditions (Hrapko et al., 2008). An additional MRE constraint is low spatial resolution resulting from methodological

limitations in MRE signal acquisition and solution of the inverse problem. Biological tissue MRE resolution is limited to ~1 mm scales, so there is a gap in spatial resolution between MRE voxels in WM and axons and near micron diameters. This results in smoothing out local mechanical property gradients (Johnson et al., 2013b; Solamen et al., 2018), or under-estimating the mechanical contributions of WM components (Urbanski et al., 2019). MRE measurements reflect voxel-averaged (effective) properties, and the solution of the inverse problem relies on constitutive tissue models to account for the microstructure and intrinsic properties of the components in each WM voxel (axons and glial cells). By focusing on the contribution of individual realistic axons to a homogenized tissue model, the present work is the first step towards formulating appropriate constitutive models by bridging the spatial scales gap.

Prior brain MRE studies (Murphy et al., 2019) are based on a priori constitutive models of the brain, which represent the brain as a heterogeneous, linear viscoelastic, and isotropic continuum. The isotropic MRE material model returns a single property pair (stiffness or storage modulus, G', and loss modulus, G''), and thus is inadequate for separating contributions to effective tissue properties from axons and glia, or their interface. There have been many indications that WM is mechanically anisotropic under shear on the mm scale, especially in regions with high directional coherence, such as the brainstem (Arbogast and Margulies, 1998), and the corpus callosum and corona radiata (Feng et al., 2013; Velardi et al., 2006). The spatial resolution and accuracy of in vivo brain MRE has recently increased, first achieving 2 mm (Johnson et al., 2013a; Johnson et al., 2013b; McGarry et al., 2013; McGarry et al., 2012) and then 1.6 mm isotropic voxels (Johnson et al., 2014). By separately exciting the brain in two different directions, the consequences of the mechanical anisotropy of WM on MRE metrics have been shown to be very important (Anderson et al., 2016). Isotropic inversions of the two separate displacement fields resulted in disparate mechanical property maps between the excitations in highly aligned WM regions. Specifically, reconstruction of G' and G" in the corpus callosum, corona radiata, and superior longitudinal fasciculus, revealed property differences between excitations of up to 33%. The need to choose the "correct" WM constitutive model for the inversion of MRE data has thus emerged. Gallo et al. (Gallo, 2020) employed high-resolution, multi-excitation MRE and a novel anisotropic inversion scheme to extract local shear anisotropic moduli from in vivo brain. It was found that the ratio of transverse to axial moduli, a new MRE metric, remains greater than 1 along all regions of the corpus callosum.

We focus here on developing a WM tissue model for MRE starting from the micromechanics of each phase. A candidate micromechanical model of WM involves a biphasic composite with aligned fibers (representing axons) embedded in a homogeneous glial matrix. The proposed canonical topology can be extended to mimic realistic WM cytoarchitecture in the spinal cord (Singh et al., 2015) or brain (Lee et al., 2019). Several micromechanical studies have modeled individual WM axons embedded in glial matrix and simulated their response to various mechanical loads using the embedded finite element technique. The choice of representative volume element (REV), kinematics, and constitutive law is based on micro-geometry and loading conditions. For very slow mechanical loading, Ogden hyperelastic models have been employed to simulate the response of WM as biphasic composites (Karami et al., 2009; Yousefsani et al., 2018a; Yousefsani et al., 2018b), which were calibrated against experiments (Meaney, 2003; Velardi et al., 2006). Embedded finite elements employed simulating affine kinematics, i.e., the axon interface is perfectly bonded to the glial matrix, so the matrix dictates its movement, to model the mechanics of the biphasic (axon-glial) composite model. Microscopic observations have revealed that axons do not demonstrate pure affine or non-affine behavior but instead transition from non-affine-dominated kinematics to affine kinematics with WM stretch level and development (Bain et al., 2003; Singh et al., 2015). To model these more realistic interfacial mechanics, we introduced a transitional kinematic model to simulate the axonal behavior within a white matter tissue subjected to uniaxial tensile stretch (Pan et al., 2011). Using an isotropic Ogden hyperelastic material model calibrated with experimental data (Meaney, 2003; Shreiber et al., 2009), adjustable "tie" constraints were applied to model axon-glial coupling with varying degrees of undulation in periodic revs. In a follow-up study (Pan et al., 2013), a pseudo-3D model was proposed to accommodate multiple axons, in addition to axon undulation and transitional kinematic model. a numerical virtual test coupled with experimental data were used to determine the transversely isotropic hyperelastic response (Pan et al., 2021). The model can accommodate large deformations and was applied to transversely isotropic spinal cord WM.

In a In a recent computational study, we considered a 2D triphasic unidirectional composite model of WM, consisting of parallel cylindrical inclusions (axons) surrounded by sheaths (myelin) and embedded in a homogeneous matrix (glial cells plus extracellular matrix), and the whole composite under pure shear perpendicular to the axon axis (Sullivan et al., 2021). Each phase was modeled by a linear viscoelastic constitutive law and was assigned uniform intrinsic (phasic) moduli G' and G''. Based on harmonic shear excitation and steady-state diffusion in the plane

perpendicular to the axon direction, a global sensitivity analysis of MRE metrics (effective transverse shear storage and loss moduli) and diffusion MRI metric (effective radial diffusivity) was performed for a wide range of microstructural (fiber volume fraction and the myelin sheath/axon diameter ratio), and intrinsic (G', G'', and diffusion coefficients) properties. The study concluded that isotropic MRE and diffusion MRI constitutive models are good approximations for myelinated WM sheared in the transverse plane. The present work builds on the above model by integrating local "micro-models" into a larger WM domain on the mesoscale.

There is no published study (to our knowledge) of 3D micromechanical models of WM tissue as a biphasic (glia-myelinated axons) composite under harmonic shear. There are no studies where actual (i.e., extracted from histology) WM micro-geometries have been employed for loading conditions pertinent to MRE. The present study proposes merging an assembly of micro-scale 3D REVs to construct an integrated mesoscale WM finite element model. Employing geometric information extracted via high-resolution imaging techniques (Singh et al., 2015), we use the local axon orientation in the CNS to study the mechanics of a mesoscopic tissue block consisting of two axons. This tissue block is subjected to harmonic shear to extract homogenized viscoelastic properties on the mesoscale (the forward problem). This homogenization is the basis of developing a constitutive material model that can be used to interpret measurements from MRE or other experimental modalities and probe the mechanical properties of individual WM constituents (by solving the inverse problem). The scope of the present work is limited to the forward problem.

2. MATERIALS AND METHODS

2.1 Microscopic REV model

A periodic representative Volume elemental (REV) is employed, consisting of a unidirectional biphasic composite of axonal fibers embedded in a homogeneous glial phase, as shown in Figure 1(a). For clarity, we call the biological data axons and their computational reconstructions axonal fibers. A local coordinate system marked by xyz is attached to each REV. The axon-aligned axes are along the z-direction of the local coordinate system congruent to the geometric distributions/constraints asserted by 1-um thick slices of CNS data (Singh et al., 2015). In contrast, the global coordinate system is marked by XYZ and identifies the loading direction. The glial phase consists of glial cells and a much softer extracellular matrix comprised of glycosaminoglycans and proteoglycans (Ruoslahti, 1996). The focus of this work is the 3D multiscale modeling of white matter consisting of arrays of curved axons. In this context, the following assumptions enhance the computational efficiency of our algorithms without oversimplifying or diminishing the novel contribution of this work. For simplicity, we assume axonal fibers of identical circular cross-sections and their conformance to a uniform hexagonal mesh (Recchia et al., 2015). Accordingly, the dominant geometrical parameter describing the microstructure is the volume fraction (VF), defined by the percentage of REV volume occupied by the axons. The size of the hexagon mesh (distance between nodes) is equal to $\alpha =$ $2 r_{fiber} \sqrt{1.75/(2\sqrt{3} VF)}$, where r_{fiber} is the axonal fiber radius. The REV shown in Figure 1(a) is the basic packing cell that can be translated in the plane transverse to the fiber axis by 2α and $\sqrt{3}\alpha$, depending on the original orientation. Without loss of generality, each phase is modeled as an isotropic continuum with uniform viscoelastic moduli, with values based on interpolation of brainstem measurements at 50Hz (Arbogast and Margulies, 1999): $G'_{axon} = 2.15 \text{ kPa}, G''_{axon} = 1.75 \text{ kPa}, G'_{glia} = 0.85 \text{ kPa}, \text{ and } G''_{glia} = 0.3 \text{ kPa}.$ The Poisson ratio of each phase was fixed at $\nu = 0.49$, representing near incompressibility of the material. Computations were performed for a volume fraction range 0.05 < VF < 0.85, with VF increments of 0.05 for each step. Note that for hexagonal packing, the maximum $VF = \frac{\sqrt{3}\pi}{6} \sim 0.9069$. According to these material properties, the orthotropic storage and loss modulus compliance tensors are calculated from the REV finite element analysis (Wu et al., 2019) (Wu et al., 2021) based on Eqs. (1)-(2), and consecutively used as the input data of the WM model.

The 3D mechanical harmonic response of the composite under six cases (axial XX-, YY-, and ZZ-, and shear XY-, XZ-, YZ-directions) of macroscopic 1% strain at 50 HZ was calculated using ABAQUS 6.14 and Python scripting. The REV was meshed with 8-node biquadratic hybrid elements resulting in a range of elements from ~5,500 to ~43,000 depending on the *VF* under consideration. The load was applied as a displacement boundary condition on the appropriate surface nodes. The faces in the REV boundary planes are assigned a repeated boundary condition, where each node's displacement is matched to a corresponding node on the opposing face. Normal force transmission is assumed at the axon-glial interface. A direct steady-state dynamic solver is used to give the response of the REV under a steady harmonic load of 50 Hz. After the steady-state harmonic field is computed, the reaction forces necessary to

result in the assigned displacements are measured and summed for each face, and the resulting average complex stress is found. The effective viscoelastic material properties of the microscopic REV are derived by dividing the (average complex) stress by 1% strain.

The effective moduli (S^*) of the homogenized REV is composed of the storage (S') and loss (S'') compliance tensors which depend on the intrinsic material properties of each phase, namely, Young's moduli, E_{ij} , shear moduli, G_{ij} , and Poisson's ratios, v_{ij} . Note that the indices ij conform with the tensor notation convention. The effective modulus of the homogenized REV is composed of the storage compliance tensor (S') and the loss compliance tensor (S''), which are defined as follows:

$$S'|_{VF} = \begin{bmatrix} \frac{1}{E'_{11}} & -\frac{v'_{21}}{E'_{22}} & -\frac{v'_{31}}{E'_{33}} \\ -\frac{v'_{12}}{E'_{11}} & \frac{1}{E'_{22}} & -\frac{v'_{32}}{E'_{33}} \\ -\frac{v'_{13}}{E'_{11}} & -\frac{v'_{23}}{E'_{22}} & \frac{1}{E'_{33}} \\ & & \frac{1}{G'_{12}} \\ & & & \frac{1}{G'_{23}} \end{bmatrix}, \tag{1}$$

$$S''|_{VF} = \begin{bmatrix} \frac{1}{E_{11}''} & -\frac{v_{21}''}{E_{22}''} & -\frac{v_{31}''}{E_{33}''} \\ -\frac{v_{12}''}{E_{11}''} & \frac{1}{E_{22}''} & -\frac{v_{32}''}{E_{33}''} \\ -\frac{v_{13}''}{E_{11}''} & -\frac{v_{23}''}{E_{22}''} & \frac{1}{E_{33}''} \\ & & \frac{1}{G_{12}''} \\ & & & \frac{1}{G_{12}''} \end{bmatrix},$$

$$(2)$$

The compliance matrix of the REV, S^* , representing the constitutive relationship of REVs, is then written per (Findley and Davis, 2013) as

$$S^* = S'|_{VF} + i S''|_{VF} = \frac{\varepsilon|_{VF}}{\sigma|_{VF}}$$
(3)

where $i = \sqrt{-1}$ is the imaginary unit, and ε and σ are the frequency-dependent strain and stress tensors, respectively, and VF-specific. Since the intrinsic moduli are fixed, the loss and storage moduli compliance tensors are only functions of VF. The effective complex stiffness (S^*) of the REV can be calculated by the storage stiffness tensor (S') and the loss stiffness tensor (S'') in Eq. (3). A similar approach provides the REV's effective complex stiffness (C^*) in Eq. (4). Similarly, based on the convention used for stress and strain components in ABAQUS, the effective stiffness matrix, C^* , of the homogenized REV, at a specific volume fraction can be calculated

$$C^* = C'|_{VF} + i C''|_{VF} = \frac{\varepsilon|_{VF}}{\sigma|_{VF}}$$
(4)

2.2 Mesoscopic White Matter (WM) Model

The computational domain of the mesoscopic WM model is constructed by assembling multiple microscopic REVs (Wu et al., 2019) (Wu et al., 2021) according to the location and orientation of individual *axons* as prescribed by 3D histological data (Singh et al., 2015). Each *axonal fiber* is located in the glia domain and is oriented in space according to 3D confocal imaging reconstruction data of embryonic chick *axonal track* data (Singh et al., 2015). Since confocal microscopy captures discrete position data at different depths along the *axonal tracks* of the examined spinal cords, additional geometric processing is necessary to recreate a smooth representation of *axonal fibers* with finite volume.

The mesoscopic model inherits the material properties of the REVs according to the local orientation of axonal fibers and the local VF. First, the discrete coordinate points of each axonal fiber, which correspond to the histologically determined centroids of the axon cross-sections, are connected to build a smooth axonal fiber spline using a curvefitting algorithm built-in ABAQUS. In particular, the axons were immunostained (Singh et al., 2015) and their topology was captured with an Olympus IX81 inverted epifluorescent microscope equipped with a confocal unit and a Hamamatsuy ImageEM digital camera. Location and time sequences of sections of 20-40 axons were traced and recorded using ImageJ. Their tortuosity, an indicator of the local architecture, was determined based on the ratio of their arc length over total length. Once the axons' 3D architecture is defined, the axons' position data are discretized in 3D space to build axonal fibers using a curve fitting algorithm in Abaqus. Then, the numerical values of tangents were extracted from the axons' traces, based on target points on each tract, to specify the material orientation at the center of each RVE (Wu et al., 2019), as shown in Figure 1(b). The material orientation of each element was calculated based on the tangent direction of its axonal fiber spline. The orientation vectors of an element are located on its centroid; thus, there is always a distance between the centroid of the element and the axonal fiber spline. Each element's orientation is influenced by the surrounding *fibers'* splines, establishing the distance between elements' centroids and axonal fiber splines as an important factor in the material orientation of each element. Because this procedure is computationally expensive, a more efficient approach is needed to assign its corresponding material orientation to every element.

We employ a 3D Radial Basis Function (RBF) interpolation method to generate material orientation for every element. *Axonal fiber* tangents can be decomposed into three different orientation components in space. As such, three RBF interpolation functions are used, one for each material orientation. Then the center points of every element associated with different directional components (Wu et al., 2019) are combined to produce the final material orientation of *axonal fiber* element in each REV. The RBF interpolation is based on computing the distance of two points in n-dimensional space defined by the function (Scala, 2017), (Fornberg, 2005):

$$f(\mathbf{x}) = \sum_{i=1}^{N} \lambda_i \phi(\|\mathbf{x} - \mathbf{x}_i\|_2) = \sum_{i=1}^{N} \lambda_i \phi(r_i),$$
 (5)

where $r_i = \|x - x_i\|_2 = \sqrt[2]{(x - x_i)^2 + (y - y_i)^2 + (z - z_i)^2}$ is the distance between x and x_i for i^{th} points, x = (x, y, z) are coordinate locations in 3D space, λ_i is weight parameter to be computed, $\phi(r_i)$ is RBF which may have numerous forms. x is the centroid of the element needed to predict the material orientation, while x_i are the locations of the tangent directions on the *axonal fiber* splines that surround x. The function output f(x) in Eq. (5) represents the material orientation of the element with centroid x.

The weight parameters, λ_i , of the interpolation function of Eq. (5) are obtained by training the associated parameters of the (x_i, h_i) data set into function f(x) where h_i are associated with values to be interpolated and x_i are point coordinates. The computation of the material orientation uses RBF interpolation to identify first the points and their associated tangents on each axonal fiber. These are selected as the input training data of 3D-RBF interpolation. The tangents have three different direction components (h_i^x, h_i^y, h_i^z) for the x, y, z direction in 3D space) resulting in three RBF interpolation functions. Then, the centroid of every element is used as input on the testing data set, and the three direction components are calculated and combined into the material orientation vector of each element. After

those two processes, every WM model element has its tensorial orientation computed based on RBF interpolation. We compared different RBFs (gaussian, inverse, multiquadric, cubic, and linear) in our data set and the linear distant RBF $\phi(r_i) = r_i$ performs better than the other methods, i.e., increased converging versus oversampling.

The VF calculation hinges on the geometry of each $axonal\ fiber$ and its location in the glia. The goal is to compute the volume intersection between $axonal\ fibers$ and the associated finite elements, as shown in Figure 1(c). The volume intersection depends on the geometry of each $axonal\ fiber$, i.e., local position vector v, tangent vector t, normal vector t, and curvature t, at the closest point. t the point on the t that exhibits the shortest distance to the center of the element. The local position vector, t, is the vector from the element's centroid to the t axonal t the closest point. The tangent, t, and normal, t, vectors specify the tangent and the normal vectors at the closest point, respectively. The curvature, t, is calculated at the closest point of the t axonal t fiber. To construct the above relationships between t and t axonal t fiber geometric information, and predict the t for the REVs, a multiple variable Support Vector Machine (SVM) algorithm is applied on the regression task.

In preparation for the training data of SVM, 2,000 axonal fibers are randomly generated and located close to a cube. The sample size increases gradually until it reaches 2,000 fibers; further, an increase in the sample size does not improve the performance of the training models tested and documented ((Pelegri et al., 2019) (Wu and Pelegri, 2020)). The random generation process supports the input feature of SVM, which is the axonal fiber geometry comprised of the local position vector, v, tangent vector, t, normal vector, n, and the curvature, c, of the axonal fiber on the closest point as the input part of a training set. The output result for each training set is the VF calculated as the ratio of (axonal fiber volume)/(cube volume). The input features and output results are computed using an internal function of ABAQUS python API. The ground truth in the training set combines the VF (prediction value) and the v, t, n, c (features) parameters. The ground truth value for the VF is the "getSize" function in ABAQUS, which returns a floating point indicating the volume of the specific geometric body. The values for the v, t, n, and c parameters are referenced by the "getCurvature" function in ABAQUS, which returns 'evaluationPoint', 'curvature', 'radius', and 'tangent'. Based on the input feature and output results, we formulate a functional SVM model describing the dependence of the volume fraction on geometric and location parameters, see Eq. (6). 67% of the 2,000 samples are used in the training process of SVM. The remaining 33% of the 2,000 samples are appropriated as a testing set. In the data preprocessing step, Standard Scaler is used for the local position vector, v, and Min Max Scaler is used for the remaining features.

$$VF = SVM(v, t, n, c), \tag{6}$$

In the validation process, the 5-fold cross-validation method (Pedregosa, F. et al., 2011) was used for the training set. Mean squared error (MSE) and mean absolute error (MAE) are selected as the evaluation metrics. The average value of 5-fold cross-validation in the training set is 0.0028 when using MSE metrics and 0.0458 when using MAE metrics. Note that MSE measures the variance of the residuals while MAE measures the average of the residuals in the dataset. The smaller the MSE and MAE, the better model's prediction capability.

In machine learning, a baseline model is required to compare with the current model. During tuning, the process of iteratively updating the current model to maximize its performance without overfitting or creating high variance, the updated new model's performance cannot be lower than the baseline's; otherwise, the latest update should be abandoned. The baseline model used here is Ridge regression. In addition, the results were treated with XHBoost to compare the model performance. In the testing set, the MSE of SVM is 98% and 42% better than the Ridge regression and the XGBoost model performances, see Figure 2. The MAE of SVM is 86% and 29% better than Ridge regression and XGBoost. The coefficient of determination value is 0.95 and 0.96 for the 5-fold cross-validation and testing data set predictions, respectively. The coefficient of determination measures how well the regression model can predict the unseen samples. It ranges from 0 (worst) to 1 (best) and is used as a metric for regression models.

The main WM modeling process is completed once the orthotropic viscoelastic material properties, orientation, and VF computation are combined (see Figure 3). The REV modeling generates the orthotropic viscoelastic material properties based on different VFs. A Radial Basis Function (RBF) process calculates the material orientation, and the VF is computed using the position and radius of each axonal fiber and the element's size. According to the geometric relationship between axonal fiber spline and WM elements, the final WM is assigned the correct orthotropic viscoelastic material properties with a redirected (corrected) material orientation tensor.

Figure 3 presents the algorithm for constructing the WM model using finite elements. The algorithm is composed of three key parts: orientation computed of each axon (blue boxes), VF computed by axon position (green boxes), and orthotropic viscoelastic material properties (salmon boxes), while the pink part of the algorithm represents the known input parameters. First, the blue part of the flow chat is the process of rebuilding the axonal fiber tracts. It creates the virtual fiber tracts and gets the tangent vector from each axonal fiber. Then the RBF 3D-interpolation method is used to get the material orientation for each REV. Second, the green part of the flow chart describes the derivative of the VF for each REV. The axon and matrix intersection computation results are used as training data for the machine learning model. Once trained, the machine learning model predicts the VF fraction based on different material orientations for each REV. The VFs will be used in the algorithm's viscoelastic material properties calculations (salmon color) to get the anisotropic material properties of REV. Tensile and shear loads are applied in the viscoelastic properties part (salmon color) of the flow chart in six directions to derive the anisotropic material properties of the REV. The effective stiffness matrix, C^* , of the homogenized REV, at a specific VF can be calculated. In summarizing, the blue part calculates the orientation, the green part computes the VF, and the salmon part evaluates the material properties using the VF of each REV. By combining the three key parts, the WM finite element can be built (yellow boxes). The three parts are coupled with each other so that they can be assigned to a related element in the final WM finite element model

3. RESULTS AND ANALYSIS

3.1 Validation of WM model building methodology

Before the histology-informed model simulation, a validation test is necessary to check the REVs compilation process and the construction of the WM model. The validation process entails combining the REVs with the same material properties into a homogeneous model that should have material properties consistent with a single REV. Consecutively, the homogeneous model can be viewed as a multi-axonal model of numerous REVs with the same material properties. Once the validation procedure ensures the homogeneity of the model, a heterogeneous WM model can be simulated, assuming REVs with different axonal orientations and material properties based on different *VFs*.

Three homogeneous (axon/glia composite) WM models, with homogenized material properties based on different VFs (10%, 45%, and 85%) are built for the validation tests. Each model is 20 μ m wide and has 1,000 elements (10x10x10) as seen in Figure 4 for model VF=45%, a representative example. The material orientations are homogenized and the *axonal fibers* lying along the global Z-direction. Stress tests of 0.1 kPa at 50 Hz in six directions (tensile in X-, Y-, and Z- directions, and pure shear in XY-, XZ-, and YZ-directions) are performed to derive the complete material properties tensor. The values were selected to represent MRE loading and can be alterred to accommodate other loading scenarios. Table 1 illustrates the test results of the homogenized WM material properties of the three VFs. The resulting maximum principal stress at VF = 45% in the global X-, XY-, XZ-, and Z-directions are shown in Figures 3 and 4. Volume fractions of 10% and 85% exhibit similar behavior but are not depicted here due to space limitations.

Model images (a), (c), (e), and (g) in Figure 4 illustrate the real components of the principal stress in the X-, XY-, YZ-, and Z-directions, while images (b), (d), (f), and (h) denote their imaginary counterparts. The inset illustrates ten elements along the X-direction. Note that the color variation among elemental vectors indicates the intensity of the magnitude of the stress field, and the vectors indicate the orientation of the stress field. Since the properties in each element are homogenized, the element's stress state is fully characterized by one vector positioned at its centroid. In Figure 4(a), the σ_{xx} magnitude and orientation originate from the mid-plane of the model, where the REV experiences the maximum stress (darker red area). The depiction of $i\sigma_{xx}$ in Figure 4(b) reveals the phase shift between the real and imaginary components of the stress tensor. In Figure 4(c), the τ_{xy} shear stress magnitude distribution is consistent with the loading condition, and the stress magnitude is identical in the XY-plane (notice that every10 elements along the Z-direction have the same color.) The $i\tau_{yz}$ magnitude in Figure 4(d) gradually decreases from the center to the cube's corner while the direction follows the phase shift of the imaginary stress component. (e-f) Similar stress orientation and magnitude trends to the ones in (c-d). Stress magnitude on $i\tau_{yz}$ (f) is larger than $i\tau_{xy}$ (d). (g) Similar to (a), the stress magnitude and orientation are identical. (h) The orientation and magnitude of the principal stress are more evenly distributed compared to (b).

In Figure 4(a), the real X-direction magnitude and direction components of the maximum principal stress appear identical. The stress result is consistent with the loading condition since the storage moduli reflect the loading condition in the real part. The magnitude of maximum principal stress in the imaginary part (Figure 4 (b)) shows much lower values than the real part (Figure 4(a)) caused by the frequency domain viscoelastic properties of REV. This situation also occurs in other directions: the XY-direction in Figure 4(d), the XZ-direction in Figure 4(f), and the Z-direction in Figure 4(h). The lower value of the imaginary part represents the delay effect caused by the real part loading condition. The stress directions show the separation effect (Figure 4(b)), which means the dynamic delay effect changes the stress magnitude and direction in the axon/glia composite. The stress magnitude of elements located on the sides and corners is lower than those in the center area (Figure 4(b)). This phenomenon, which is noted in directions XY Figure 4(d) and XZ Figure 4(f), and in Z-direction Figure 4(h), suggests that the elements located on the sides and corners suffer less stress caused by the delay effect than the center area elements.

The stiffness of the homogeneous model in the Z-direction should be larger than the one in X- or Y-directions since the stiffness of the axon is larger than the glia. Therefore, in the center area of Figure 4(b), the stress direction is aimed at the Y-direction rather than the axonal Z-direction. Further, it is noted that the stress is more evenly distributed in the center area of Figure 4(h), than that of Figure 4(b) due to the similar material properties of the homogeneous model in the X- and Y- directions (both vertical to the axonal Z-direction).

The real stresses components are identical in magnitude and direction as caused by pure shear stress loading as shown in Figures 4(c) and (e). The directions of the imaginary stress counterparts (Figures 4(d) and (f)) are normal to the real stress direction (Figures 4(c) and (e)). The stress magnitudes of the imaginary part subjected to tensile loading (Figures 4(b) and (h)) are much larger than shear loading (Figures 4(d) and (f)), although the loading conditions are the same. This outcome affirms that a more prominent dynamic delay effect occurs in shear loading than in tensile loading, suggesting that the axon/glia composites are more sensitive to shear loading than tensile loading. The dynamic amplitude results (Figures 5(a)-(d)) indicate nearly equivalent results with the real part result (Figures 4(a), (c), (e) and (g)), supports the finding that the storage (real) component of the stress is more prominent than the loss (imaginary) one in dynamic loading.

Validation test results are presented in Table 1 where the original orthotropic material properties of the REVs and test material properties (C_{ij} , i = 1,2...6 and j = 1,2...6) of the homogeneous models are listed. The values of C_{ij} are the elements of the stiffness tensor (the inverse of compliance tensor in Equations (1)-(2)). The homogeneous WM model is constructed with multiple REVs with the same axonal orientation and VF. Validation tests illustrate that the WM model has the same material properties with a single REV when the orientation and the VF of multiple REVs within the WM model are the same. The next step is to use the REVs with various VF and axonal orientations to construct the general WM model.

3.2 Effective properties computation of WM model

The WM model simulation selects the location coordinates of two axonal traces in 3D space as input information per Singh et al., 2015, 2017). Consequently, the axonal trace geometry can be generated using the spline method in ABAQUS 6.14 and Python scripting following (Wu et al., 2019). The modeling process is based on the methodology shown in Figure 5 and is coded in Python 2.7. The WM model is made up of 4,320 elements, and in Figure 6 the grids of the internal elements are hidden to reveal the axonal fiber structure. The material orientations (blue arrows), follow closely the direction of the axonal traces (red splines). The orthotropic elements of various *VFs* are surrounded by axonal traces, which depend on the distance between elements and axonal traces. Therefore, the WM model involves an assembly of various REVs with related *VF* and material properties. Each element has the same edge length of 20 µm but different *VF* according to its distance to the axonal trace. A homogenized radius of 15µm, representing the two 7µm axons (Singh et al., 2015) in REV, see Figure 1(a), is assumed for the virtual axonal traces and is used to calculate the *VF* of the elements surrounded by them. For example, any element in Figure 6 without any blue arrows has a *VF* equal to one and indicates an element of pure glia. Other elements have different *VFs*, ranging from 5% to 85%.

The stress magnitudes and directions of the WM model subjected to 0.01 tensile strain at 50 Hz frequency are depicted in Figure 7(a) for local stress, σ_{33} , and Figure 7(b) for local maximum principal stress. The direction of local stresses, σ_{33} , is followed by the original axonal traces' direction. The higher stress magnitude regions focus on the

axonal traces of Figures 7(a)-(b) are shown as red arrows, indicating that the axonal trace to element distance is a significant factor for stress magnitude distribution, as higher VF ratio elements are nearby the axonal traces. Higher VF ratio elements are stiffer, which corroborates the in-vivo conditions of WM. Comparison of Figures 7(a)-(b) shows that the maximum principal stresses have similar direction and magnitude distributions with the local stresses, σ_{33} . The latter further supports that axonal trace structures and orientation significantly impact dynamic WM simulation and stress-strain response. The maximum principal stress in each element is depicted by arrows along the direction of the axonal traces in Figure 8. The green cubes signify that the elements with $50\% \le VF$ (Figure 8 (a)) and the elements $0\% \le VF < 50\%$ (Figure 8 (b)) are concentrated around the axonal traces. The stresses concentrate around the elements close to axonal traces' locations inside the WM.

4. DISCUSSION

4.1 Originality and importance of the mesoscopic WM model development

Driven by the need to model accurately the harmonic response of WM and to interpret elastography data, this work focused on developing a multiscale WM tissue model starting from the microstructure, which in our case is reconstructed from optical microscopy. Here we construct a histology-informed model that can simulate the intrinsic properties at the cellular level (axon, glial matrix), and interpret MRE data at the tissue level under a dynamic load that simulates MRE conditions. The originality of this work lies with the efficiency and sophistication of the multiscale model that bridges the microscale (single axon) with the mesoscale (group of axons). Sets of anisotropic REVs are assembled to describe curved axons in 3D space, thus eliminating the need to create complicated partitions of the finite element grids, as is the case with traditional composite finite element methods. Each REV contains a hexagonal periodic array of axons, coupled via slip to the glial matrix. The WM model expresses a combination method that includes various REVs with related *VF* and material properties. In addition, each element with the same edge length of 20 µm has a different *VF* according to the distance from the element to the axonal trace.

At the microscale, the model involves a direct simulation of the harmonic response of a biphasic composite with axonal fibers, which are generally oriented in the same (main) direction and are embedded in a homogeneous glial matrix. Local architecture, i.e., axon fiber alignment relative to the main direction, diameter, and volume fraction, affects the constitutive response of neural tissue to normal stresses (Koser et al., 2015). At this scale, the present model is an extension of the model of Sullivan et al. (2021), where only the transverse direction was considered, and the transverse effective shear moduli were calculated. Based on a 2D triphasic composite tissue model consisting of a periodic array of axons, the Sullivan et al. study revealed high sensitivity of the effective (homogenized) REV mechanical properties to the fiber volume fraction, and the intrinsic viscoelastic moduli of the glial phase. The extension of the (Sullivan et al. 2021) model to 3D is reported in (Wu et al. 2021) who studied the 3D response to shear load in transverse (yz- and xz-planes) and axial (xy-plane) directions, see Figure 1. Wu et al. (2021) demonstrated consistency of stress distribution between the 2D REV and 3D REV models in the axial plane (parallel to the fiber direction). Furthermore, our models were validated by comparing with exact transverse moduli calculations based on (Christensen, 2005). Both 2D and 3D models rely on composites consisting of homogeneous phases. The above work bolsters the hypothesis that mechanical anisotropy is intimately related to the intrinsic mechanical properties of each phase and the geometrical arrangement of each phase.

The presented work is the first step towards developing a realistic 3D simulation framework for performing MRE-DTI *in silico* experiments in complex, histology-based WM domains (the forward problem). The benefits of this endeavor are multifold. First, this will further inform the selection of the appropriate constitutive model for solving the inverse problem in MRE. Second, this 3D WM framework will constitute a sophisticated numerical phantom for brain microstructural MRI (Fieremans and Lee, 2018). For example, cellular biomechanics can be readily incorporated in our composite model to explore the underlying mechanisms of rapid changes of WM elasticity (Patz et al., 2019). The high sensitivity of MRE metrics to glial properties reported here might provide useful insights into the observed stiffness variations. Third, it will enable the integration of new knowledge regarding the mechanical failure of axons (Abolfathi et al., 2009; Singh et al., 2017) (Montanino and Kleiven, 2018) in neuroimaging studies of traumatic brain injury (Eierud et al., 2014). Fourth, it will allow the incorporation of multi-scale datasets, both *in vivo* and *ex vivo*, towards creating a structural framework for the systematic study of whole brain circuits (Muñoz-Castañeda et al., 2021).

4.2 Effective viscoelastic properties of the mesoscopic WM model

The present study is based on a composite medium containing two axonal fibers, whose geometry is reconstructed from sections of the chicken ventral spinal cord (Singh et al. 2015). As shown in Figure 6, the numerical domain consists of 4320 elements, each corresponding to a physical cube size of 20 x 20 x 20 µm. The fiber volume fraction (VF) is extended and ranges from 5% to 85%. The fibers are oriented along the main direction Z. The mean and standard deviation of the angle between the axonal trace tangent and Z-direction are $\bar{\theta}$ =27.81°, $\sigma(\theta)$ =11.06° for axon-1, and $\bar{\theta}$ =25.47°, $\sigma(\theta)$ =11.67° for axon-2, respectively. This level of dispersion of the local orientation angle is consistent with levels that have been measured in other oriented white matter regions of the brain, i.e., the corpus callosum (Lee et al., 2019). With the fibers not perfectly aligned along Z and this level of angle dispersion, the present results demonstrate that in terms of its mechanical behavior, the composite is anisotropic (orthotropic) with Z as the major axis.

The equivalent homogenized behavior of the REV is approximated by a transversely isotropic model, under both axial and shear loading ($C'_{44} \neq C'_{55} \sim C'_{66}$). This anisotropy has been replicated in all prior micromechanical studies of WM used viscoelastic constitutive laws (Abolfathi et al., 2009; Javid et al., 2014), which is expected since it is reflected in the experimental data used to calibrate the models (Arbogast and Margulies, 1999; Meaney, 2003). Recent measurements of directional Young's moduli of mice spinal cords revealed that WM behaves like a transversely isotropic material under compression, and an almost isotropic material under tension (Koser et al., 2015). Systematic measurements of the viscoelastic responses of small arrays of axons are lacking. Our results show that the stress magnitudes of the imaginary part subjected to tensile loading (Figures 4(b) and (h)) are much larger than shear loading (Figures 4(d) and (f)), although the loading conditions are the same. This outcome affirms that a more prominent dynamic delay effect occurs in shear loading than in tensile loading, suggesting that the axon/glia composites are more sensitive to shear loading than tensile loading.

As seen in Table 1, the transverse shear storage modulus (Figure 4e) is always larger than the parallel storage modulus (Figure 4c) $C'_{44}/C'_{55} > 1$, with the ratio increasing as VF increases. This trend is consistent with the fact that the axon stiffness is higher than the glial. Wu et al. (2021) concluded that the ratio of transverse to axial transverse modulus is larger than one in that case. With the exception of one study (Budday et al., 2017), this shear anisotropy has also been reported in $ex\ vivo$ brain WM experiments but with $C'_{44}/C'_{55} < 1$. On one hand the experimental results indicate $C'_{44}/C'_{55} > 1$ for porcine brainstem (Arbogast and Margulies, 1998) and porcine corpus callosum (Prange and Margulies, 2002), and on the other hand, $C'_{44}/C'_{55} < 1$ for porcine corona radiata (Prange and Margulies, 2002) and porcine corpus callosum (Feng et al., 2013; Schmidt et al., 2018). In a recent review (Budday et al., 2019), this inconsistency was assigned to microstructure inhomogeneity and experimental artifacts related to exposing the excised WM tissue specimens to harmonic rectilinear shear.

In vivo measurements of WM mechanical properties currently rely on elastography. In vivo measurements via MRE provide unequivocal support that brain WM is transversely isotropic in shear. Nevertheless, past MRE measurements are equivocal as to which direction dominates. For example, it was reported that $C'_{44}/C'_{55} > 1$ for human corticospinal tracts (Romano et al., 2014; Romano et al., 2012), while $C'_{44}/C'_{55} < 1$ was found for the corpus callosum (Smith et al., 2020) The present study supports the finding that $C'_{44}/C'_{55} > 1$, and other than the geometric simplifications involved in defining the REV, is devoid of experimental artifacts. These predictions agree with recent MRE work (Gallo et al 2020), whereby a transversely isotropic constitutive model for the brain WM was used to interpret prior experiments involving 7 young and 4 older healthy men. By employing a novel inversion scheme, it was found that the effective transverse shear moduli remain higher than the axial moduli in two well-aligned WM structures, namely in the corpus callosum and corticospinal tracts. The present multiscale methodology (hexagonal packing of axons in REV, and consecutive histology informed mesoscale homogenization) can predict the transverse anisotropy of WM for a large range of VFs (5-85%) at dynamic loading of 50 Hz. This is of the outmost importance because we can now accurately simulate intricate intrinsic microstructures (curved and tortuous axons, replicate boundary conditions) and create homogenized models that extend to the mm-scale voxels. At this scale we can directly compare with MRE data, and we can cross validate with DTI studies.

4.3 Limitations of the current study

Some of the limitations of this study are related to the morphological description of the WM microstructure. The present study considers REVs with periodic hexagonal arrangement of parallel identical fibers that are in contact with the glial matrix but can slip relative to the interface. The hexagonal arrangement of the fibers results in transversely isotropic behavior of the equivalent homogenized REV. Considering other arrangements and fiber/glial interfacial conditions alters the REV symmetry, and the effective properties defined in Equations (1-2). Square or random packings of identical cylinders create orthotropic REVs, with the shear moduli increasing as follows square<hexagonal<random for each VF value (Huang et al., 2008). This observation also holds for the case of random diameter distribution (Abolfathi et al., 2009). The axonal fibers have identical circular cross-sections, and they conform to a uniform hexagonal mesh. For the interested reader, random distribution of axonal diameters in this model can be incorporated following the work of Recchia et al. (2015).

Additional limitations stem from the topology and mechanical coupling between the phases. In Sullivan at al. (2021), the REV included three phases, axon, myelin, and glial matrix but the sensitivity analysis revealed that the glial matrix properties have the strongest effect on the effective shear response of the homogenized REV. Therefore, we opted for lumping the two phases (axon and myelin) into one phase. Increasing the bonding between the phases increases the effective shear moduli, at least for hexagonal packing (Devries, 1993), so the moduli predictions reported here can be considered a lower bound. Another limitation is the assumption that the glial phase is homogeneous. The lack of granularity in the glia matrix is a result of the dearth of 3D glia cell reconstructions, as well as the short-range order of these cells. Should reconstructions of glial cells become available, our method can accommodate them. Taken together the above results imply that the methodology can accommodate any variations of geometry or property to make a more realistic interpretation of experiments that are accompanied by histology-based microstructural measurements.

5. CONCLUSIONS

Modeling traumatic injuries of the brain and spinal cord requires the extraction of tissue mechanical properties. Non-invasive techniques, such as Magnetic Resonance Elastography (MRE), can be used to probe the mechanical properties of white matter (WM) but their interpretation requires the development of constitutive tissue models that depend on efficient mathematical representations of the architecture and intrinsic properties of the tissue. Scaledependent anisotropy of white matter geometry and heterogeneous material properties complicate the direct numerical simulations of its viscoelastic response. In classical finite element methods, discretization of complex axon-glial matrix assemblies requires complicated, custom-made partitions of the finite element grids and make the simulation cumbersome. To obviate this difficulty, an economic homogenization scheme based on the micro- and mesoscale was developed. A 3D model that accounts for the anisotropy introduced by the axon/neuroglia composite, axonal trace curvature, and tissue dynamic response in the frequency domain is presented. To describe curved axons in 3D space, the micromechanical model of WM involves assembling multiple REVs of a biphasic composite with aligned fibers (representing axons) embedded in a homogeneous glial matrix. Each REV entails hexagonal packing of axons and is described by a local axon direction and volume fraction, along with the material properties of the constituent phases. The mesoscale model is built by assembling these anisotropic REVs with fiber volume fractions depending on the distance from the axonal trace. Three fiber volume fractions 10%, 45%, and 85%, and six loading scenarios, three tensile and three pure shear, were simulated under MRI dynamic load conditions (small strain, 50 Hz). The full anisotropic material properties tensor was calculated and validated. It was observed that a more prominent dynamic delay effect occurs in shear loading than in tensile loading, suggesting that the axon/glia composites are more sensitive to shear loading than tensile loading.

Geometric parameters extracted from microscopy studies of optical nerve histology were used for the histology-informed WM model simulation. The model consists of two axons from embryonic chick spinal cord (Singh et al., 2015). The selection and incorporation of only 2 axons does not reduce the generality of our approach. Stress fields were studied on the microscale and effective shear moduli on the mesoscale. The important findings are as follows: First, the stress magnitudes and directions of the WM are strongly influenced by axonal trace location changes when subjected to tension. Second, effective shear moduli perpendicular to the "average" axon direction are higher than along that direction. The first result provides a justification for pursuing multiscale models for WM; they are

indispensable when axon failure modes are studied. The second result addresses the ongoing controversy of WM anisotropy measured by MRE.

The presented multiscale methodology (REV and histology-informed mesoscale homogenization) can predict the transverse anisotropy of WM for a large range of VFs (5-85%) at dynamic loading of 50 Hz. This is of the outmost importance because we can now accurately simulate intricate intrinsic microstructures (curved and tortuous axons, replicate boundary conditions) and create homogenized models that extend to the mm-scale voxels. At this scale we can directly compare with MRE data, and we can cross validate with DTI studies. Since our methodology does not rely on analytical homogenization techniques, it is flexible enough to accommodate more sophisticated microstructural models by modifying the micromechanics of the REVs. For example, the platform can easily accommodate intra-axonal mechanics, more cellular components, and the effects of different loading and test conditions to allow comparisons with ex-vivo or in-vivo studies of WM. This novel approach enables the concurrent incorporation of local architecture, material, and scaling factors to accurately simulate white matter viscoelastic behavior subjected to dynamic loading. The model markedly predicts dynamic response of histology-informed white matter tissue when compared to simplified (non-complex) periodic models. The proposed framework is an essential step in computationally efficient but geometrically accurate representation of tissue where trauma-related structural changes can be modeled.

6. ACKNOWLEDGMENTS

Support was provided by NSF Grants CMMI-1436743, CMMI-1437113, CMMI-1762774, CMMI-1763005, and the R.A. Pritzker endowed chair.

REFERENCES

Abolfathi, N., Naik, A., Chafi, M.S., Karami, G., Ziejewski, M., 2009. A micromechanical procedure for modelling the anisotropic mechanical properties of brain white matter. Comput. Methods Biomech. Biomed. Eng. 12, 249-262.

Anderson, A.T., Van Houten, E.E., McGarry, M.D., Paulsen, K.D., Holtrop, J.L., Sutton, B.P., Georgiadis, J.G., Johnson, C.L., 2016. Observation of direction-dependent mechanical properties in the human brain with multi-excitation MR elastography. Journal of the mechanical behavior of biomedical materials 59, 538-546.

Arbogast, K.B., Margulies, S.S., 1998. Material characterization of the brainstem from oscillatory shear tests. Journal of Biomechanics 31, 801-807.

Arbogast, K.B., Margulies, S.S., 1999. A fiber-reinforced composite model of the viscoelastic behavior of the brainstem in shear. Journal of Biomechanics 32, 865-870.

Bain, A.C., Shreiber, D.I., Meaney, D.F., 2003. Modeling of microstructural kinematics during simple elongation of central nervous system tissue. Journal of biomechanical engineering 125, 798-804.

Budday, S., Ovaert, T.C., Holzapfel, G.A., Steinmann, P., Kuhl, E., 2019. Fifty Shades of Brain: A Review on the Mechanical Testing and Modeling of Brain Tissue. Archives of Computational Methods in Engineering, 1-44.

Budday, S., Sommer, G., Birkl, C., Langkammer, C., Haybaeck, J., Kohnert, J., Bauer, M., Paulsen, F., Steinmann, P., Kuhl, E., 2017. Mechanical characterization of human brain tissue. Acta biomaterialia 48, 319-340.

Chatelin, S., Constantinesco, A., Willinger, R., 2010. Fifty years of brain tissue mechanical testing: from in vitro to in vivo investigations. Biorheology 47, 255-276.

Christensen, R.M., 2005. Mechanics of Composite Materials. Dover Publications.

Devries, F., 1993. Bounds on Elastic Moduli of Unidirectional Composites with Imperfect Bondang. Composites Engineering 3, 349-382.

Eierud, C., Craddock, R.C., Fletcher, S., Aulakh, M., King-Casas, B., Kuehl, D., LaConte, S.M., 2014. Neuroimaging after mild traumatic brain injury: review and meta-analysis. NeuroImage: Clinical 4, 283-294.

Feng, Y., Okamoto, R.J., Namani, R., Genin, G.M., Bayly, P.V., 2013. Measurements of mechanical anisotropy in brain tissue and implications for transversely isotropic material models of white matter. J. Mechanical Behavior of Biomedical Materials 23, 117–132.

Fern, R., 2017. The Leukocentric Theory of Neurological Disorder: A Manifesto. Neurochemical Research 42, 2666-2672.

Fieremans, E., Lee, H.-H., 2018. Physical and numerical phantoms for the validation of brain microstructural MRI: A cookbook. Neuroimage 182, 39-61.

Findley, W.N., Davis, F.A., 2013. Creep and relaxation of nonlinear viscoelastic materials. Courier Corporation.

Fornberg, B.F., N., 2005. Accuracy of radial basis function interpolation and derivative approximations on 1-D infinite grids. Advances in Computational Mathematics 23, 5-20.

Franze, K., Janmey, P.A., Guck, J., 2013. Mechanics in Neuronal Development and Repair. Annual Review of Biomedical Engineering 15, 227-251.

Gallo, N.R.C., S.M.; Anderson, A.T.; Naughton, N.M.; Pelegri, A.A.; Georgiadis, J.G., 2020. Variation of In Vivo Anisotropic MRE Metrics in Corpus Callosum: Effect of Aging, International Society of Magnetic Resonance in Medicine Virtual, p. 0164.

Holle, A.W., Young, J.L., Van Vliet, K.J., Kamm, R.D., Discher, D., Janmey, P., Spatz, J.P., Saif, T., 2017. Cell–Extracellular Matrix Mechanobiology: Forceful Tools and Emerging Needs for Basic and Translational Research. Nano letters 18, 1-8.

Hrapko, M., van Dommelen, J.A.W., Peters, G.W.M., Wismans, J., 2008. The influence of test conditions on characterization of the mechanical properties of brain tissue. J. Biomech. Eng.-Trans. ASME 130, 10.

Huang, Y.C., Jin, K.K., Ha, S.K., 2008. Effects of fiber arrangement on mechanical behavior of unidirectional composites. Journal of Composite Materials 42, 1851-1871.

Javid, S., Rezaei, A., Karami, G., 2014. A micromechanical procedure for viscoelastic characterization of the axons and ECM of the brainstem. Journal of the Mechanical Behavior of Biomedical Materials 30, 290-299.

Johnson, C.L., Holtrop, J.L., McGarry, M.D.J., Weaver, J.B., Paulsen, K.D., Georgiadis, J.G., Sutton, B.P., 2014. 3D Multislab, Multishot Acquisition for Fast, Whole-Brain MR Elastography with High Signal-to-Noise Efficiency. Magnetic Resonance in Medicine 71, 477-485.

Johnson, C.L., McGarry, M.D.J., Gharibans, A.A., Weaver, J.B., Paulsen, K.D., Wang, H., Olivero, W.C., Sutton, B.P., Georgiadis, J.G., 2013a. Local mechanical properties of white matter structures in the human brain. Neuroimage 79, 145-152.

Johnson, C.L., McGarry, M.D.J., Van Houten, E.E.W., Weaver, J.B., Paulsen, K.D., Sutton, B.P., Georgiadis, J.G., 2013b. Magnetic resonance elastography of the brain using multishot spiral readouts with self-navigated motion correction. Magnetic Resonance in Medicine 70, 404-412.

Karami, G., Grundman, N., Abolfathi, N., Naik, A., Ziejewski, M., 2009. A micromechanical hyperelastic modeling of brain white matter under large deformation. Journal of the mechanical behavior of biomedical materials 2, 243-254.

Koser, D.E., Moeendarbary, E., Hanne, J., Kuerten, S., Franze, K., 2015. CNS cell distribution and axon orientation determine local spinal cord mechanical properties. Biophys J 108, 2137-2147.

Lamoureux, P.L., O'Toole, M.R., Heidemann, S.R., Miller, K.E., 2010. Slowing of axonal regeneration is correlated with increased axonal viscosity during aging. Bmc Neuroscience 11.

Lee, H.-H., Yaros, K., Veraart, J., Pathan, J.L., Liang, F.-X., Kim, S.G., Novikov, D.S., Fieremans, E., 2019. Along-axon diameter variation and axonal orientation dispersion revealed with 3D electron microscopy: implications for quantifying brain white matter microstructure with histology and diffusion MRI. Brain Structure and Function 224, 1469-1488.

McGarry, M.D.J., Johnson, C.L., Sutton, B.P., Georgiadis, J.G., Van Houten, E., Weaver, J.B., Paulsen, K.D., 2013. Including Spatial Information in Nonlinear Inversion MR Elastography Using Soft Prior Regularization. IEEE Trans. Medical Imaging 32, 1901-1909.

McGarry, M.D.J., Van Houten, E., Johnson, C.L., Georgiadis, J.G., Sutton, B.P., Weaver, J.B., Paulsen, K.D., 2012. Multi-resolution MR Elastography Using Non-linear Inversion. Medical Physics 39, 6388-6396.

Meaney, D.F., 2003. Relationship between structural modeling and hyperelastic material behavior: application to CNS white matter. Biomechanics and modeling in mechanobiology 1, 279-293.

Montanino, A., Kleiven, S., 2018. Utilizing a structural mechanics approach to assess the primary effects of injury loads onto the axon and its components. Frontiers in neurology, 643.

Muñoz-Castañeda, R., Zingg, B., Matho, K.S., Chen, X., Wang, Q., Foster, N.N., Li, A., Narasimhan, A., Hirokawa, K.E., Huo, B., Bannerjee, S., Korobkova, L., Park, C.S., Park, Y.-G., Bienkowski, M.S., Chon, U., Wheeler, D.W., Li, X., Wang, Y., Naeemi, M., Xie, P., Liu, L., Kelly, K., An, X., Attili, S.M., Bowman, I., Bludova, A., Cetin, A., Ding, L., Drewes, R., D'Orazi, F., Elowsky, C., Fischer, S., Galbavy, W., Gao, L., Gillis, J., Groblewski, P.A., Gou, L., Hahn, J.D., Hatfield, J.T., Hintiryan, H., Huang, J.J., Kondo, H., Kuang, X., Lesnar, P., Li, X., Li, Y., Lin, M., Lo, D., Mizrachi, J., Mok, S., Nicovich, P.R., Palaniswamy, R., Palmer, J., Qi, X., Shen, E., Sun, Y.-C., Tao, H.W., Wakemen,

W., Wang, Y., Yao, S., Yuan, J., Zhan, H., Zhu, M., Ng, L., Zhang, L.I., Lim, B.K., Hawrylycz, M., Gong, H., Gee, J.C., Kim, Y., Chung, K., Yang, X.W., Peng, H., Luo, Q., Mitra, P.P., Zador, A.M., Zeng, H., Ascoli, G.A., Josh Huang, Z., Osten, P., Harris, J.A., Dong, H.-W., 2021. Cellular anatomy of the mouse primary motor cortex. Nature 598, 159-166.

Murphy, M.C., Huston, J., Ehman, R.L., 2019. MR elastography of the brain and its application in neurological diseases. NeuroImage 187, 176-183.

Pan, Y., Shreiber, D.I., Pelegri, A.A., 2011. A Transition Model for Finite Element Simulation of Kinematics of Central Nervous System White Matter. IEEE Transactions on Biomedical Engineering 58, 3443-3446.

Pan, Y., Shreiber, D.I., Pelegri, A.A., 2021. On the Transversely Isotropic, Hyperelastic Response of Central Nervous System White Matter Using a Hybrid Approach. Journal of Engineering and Science in Medical Diagnostics and Therapy 4.

Pan, Y., Sullivan, D., Shreiber, D.I., Pelegri, A.A., 2013. Finite element modeling of CNS white matter kinematics: use of a 3D RVE to determine material properties. Frontiers in bioengineering and biotechnology 1, 19.

Patz, S., Fovargue, D., Schregel, K., Nazari, N., Palotai, M., Barbone, P.E., Fabry, B., Hammers, A., Holm, S., Kozerke, S., 2019. Imaging localized neuronal activity at fast time scales through biomechanics. Science advances 5, eaav3816.

Pelegri, A.A., Georgiadis, J.G., Wu, X., 2019. Brain White Matter Model of Orthotropic Viscoelastic Properties in Frequency Domain, Volume 3: Biomedical and Biotechnology Engineering.

Pogoda, K., Janmey, P.A., 2018. Glial tissue mechanics and mechanosensing by glial cells. Frontiers in Cellular Neuroscience 12, 25.

Prange, M.T., Margulies, S.S., 2002. Regional, directional, and age-dependent properties of the brain undergoing large deformation. Journal of biomechanical engineering 124, 244-252.

Recchia, S., Zheng, J.Q., Horner, S., Pelegri, A.A., 2015. Multiscale modeling of randomly interwoven fibers for prediction of KM2 Kevlar yarn strength and damage. Acta Mechanica 226, 4149-4158.

Romano, A., Guo, J., Prokscha, T., Meyer, T., Hirsch, S., Braun, J., Sack, I., Scheel, M., 2014. In vivo waveguide elastography: Effects of neurodegeneration in patients with amyotrophic lateral sclerosis. Magnetic Resonance in Medicine 72, 1755-1761.

Romano, A., Scheel, M., Hirsch, S., Braun, J., Sack, I., 2012. In Vivo Waveguide Elastography of White Matter Tracts in the Human Brain. Magnetic Resonance in Medicine.

Ruoslahti, E., 1996. Brain extracellular matrix. Glycobiology 6, 489-492.

Saab, A.S., Nave, K.A., 2017. Myelin dynamics: protecting and shaping neuronal functions. Curr. Opin. Neurobiol. 47, 104-112.

Scala, V., 2017. RBF Interpolation with CSRBF of Large Data Sets. Procedia Computer Science 108, 2433-2437.

Schmidt, J.L., Tweten, D.J., Badachhape, A.A., Reitera, A.J., Okamoto, R.J., Garbow, J.R., Bayly, P.V., 2018. Measurement of anisotropic mechanical properties in porcine brain white matter ex vivo using magnetic resonance elastography. Journal of the Mechanical Behavior of Biomedical Materials 79, 30-37.

Shreiber, D.I., Hao, H.L., Elias, R.A.I., 2009. Probing the influence of myelin and glia on the tensile properties of the spinal cord. Biomechanics and Modeling in Mechanobiology 8, 311-321.

Singh, S., Pelegri, A.A., Shreiber, D.I., 2015. Characterization of the three-dimensional kinematic behavior of axons in central nervous system white matter. Biomechanics and modeling in mechanobiology 14, 1303-1315.

Singh, S., Pelegri, A.A., Shreiber, D.I., 2017. Estimating axonal strain and failure following white matter stretch using contactin-associated protein as a fiduciary marker. Journal of biomechanics 51, 32-41.

Smith, D.R., Guertler, C.A., Okamoto, R.J., Romano, A.J., Bayly, P.V., Johnson, C.L., 2020. Multi-Excitation Magnetic Resonance Elastography of the Brain: Wave Propagation in Anisotropic White Matter. J Biomech Eng 142.

Solamen, L.M., McGarry, M.D., Tan, L., Weaver, J.B., Paulsen, K.D., 2018. Phantom evaluations of nonlinear inversion MR elastography. Physics in Medicine & Biology 63, 145021.

Sullivan, D.K., Wu, X., Gallo, N.R., Naughton, N.M., Georgiadis, J.G., Pelegri, A.A., 2021. Sensitivity Analysis of Effective Transverse Shear Viscoelastic and Diffusional Properties of Myelinated White Matter. Physics in Medicine & Biology 60, 035027.

Urbanski, M.M., Brendel, M.B., Melendez-Vasquez, C.V., 2019. Acute and chronic demyelinated CNS lesions exhibit opposite elastic properties. Scientific Reports 9.

Velardi, F., Fraternali, F., Angelillo, M., 2006. Anisotropic constitutive equations and experimental tensile behavior of brain tissue. Biomechanics and Modeling in Mechanobiology 5, 53-61.

Wu, X., Georgiadis, J.G., Pelegri, A.A., 2019. Brain White Matter Model of Orthotropic Viscoelastic Properties in Frequency Domain, Volume 3: Biomedical and Biotechnology Engineering; IMECE2019-12182.

Wu, X., Georgiadis, J.G., Pelegri, A.A., 2021. Biphasic Representative Elemental Volumes for 3-D White Matter Elastography, Volume 5: Biomedical and Biotechnology.

Wu, X., Pelegri, A.A., 2020. Deep 3D Convolution Neural Network Methods for Brain White Matter Hybrid Computational Simulations, Volume 5: Biomedical and Biotechnology.

Yousefsani, S.A., Farahmand, F., Shamloo, A., 2018a. A three-dimensional micromechanical model of brain white matter with histology-informed probabilistic distribution of axonal fibers. Journal of the Mechanical Behavior of Biomedical Materials 88, 288-295.

Yousefsani, S.A., Shamloo, A., Farahmand, F., 2018b. Micromechanics of brain white matter tissue: A fiber-reinforced hyperelastic model using embedded element technique. Journal of the mechanical behavior of biomedical materials 80, 194-202.

Figure Captions

- Figure 1(a) Shear stress response to XY-shear loading of microscopic biphasic white matter REV with axonal fiber surrounded by glial phase. Result at a phase angle of 0° with Von Mises stress (kPa) plotted. Axonal fibers of identical circular cross-sections are regularly distributed in hexagonal packing arrangement allowing for different packing geometries and varying mechanical interactions at axon/glial interface. b) Graphic representation of aligned orientation vectors of the finite element and axonal fiber. The pink start symbol is the centroid of this element. The pink arrow is the extracted tangent (yellow arrow) from the rebuilt axonal trace at the centroid of this element, which represents its material orientation. (c) Sample of REV training data with randomly generated VFs of 0.45, 0.67, and 0.85. The VF of this specific element will be predicted by the trained SVR model.
- Figure 2 Graphic representation of SCV training comparison. Red bar represents SVM, green represents XGBoost used for comparing with current model, and black is Ridge regression used as baseline model. MSE (variance of residuals) and MEA (average of residuals) are used to compare the three models. SVM outperforms XGBoost and Ridge (baseline model) in both comparative sets.
- Figure 3 Algorithm for constructing the WM model using finite elements. The algorithm comprises (3) key parts: orthotropic viscoelastic material properties (salmon boxes group), V_f computed by axon position (green boxes groups) and orientation (blue boxes group) of each axon. The three parts are coupled with each other so that they can be assigned to a related element in the final WM finite element model. The pink boxes indicate the know parameters (input). The yellow boxes represent the final combination of material properties, volume fraction, and orientation for each element and the assembly of the WM FEM.
- Figure 4 Representative results of maximum principal stress experienced by REV of VF = 45% subjected to 0.1 kPa in (X-, Z-, XY-, XZ-) global directions at 50 Hz frequency. Yellow arrows indicate loading directions. The axonal direction of REV is along the global Z-direction. (a) Real components and (b) Imaginary components of maximum principal stress test in X-direction. (inset) 10 sample elements in the XX-direction from real portion result of (a). Different colors denote stress distribution. (c) Real components and (d) Imaginary components of maximum principal stress test in the XY-direction. (e) Real components and (f) Imaginary components of maximum principal stress test in the XZ-direction. (g) Real components and (h) Imaginary components of maximum principal stress test in the Z-direction. Model illustrates 10 elements in the global X-, Y-, and Z-directions amounting to 1,000 elements. The stress field at the center point of each REV is marked.
- Figure 5 Dynamic amplitude results of maximum principal stress under tensile stress in (a) XX-direction, (b) XY-direction, (c) XZ-direction, and (d) ZZ-direction. Dynamic amplitude is the combination magnitude of both the real and imaginary portions of the result value. Each value is the square root of the sum of the squares of the real and imaginary invariant components. The results are analogous to the real part result of each direction in Figure 4.
- Figure 6 Mesoscopic WM model indicating axonal tract splines and material orientation in 3D space. The red splines represent the geometric axis of the axonal traces generated from axonal location coordinates data and are not included in the stress-strain analysis. There are 4,320 elements of size 20 x 20 x 20 µm each in the WM model. The material orientations in the z-direction of local

coordinate system indicated by the blue arrows on the elements that are generated from microscopic REVs. The remaining elements without material orientation represent the pure glia phase in WM. Boundary condition is 0.01 strain tensions at 50Hz frequency, shown as red arrows in positive and negative global Z-direction. Inset illustrates one of the elements with the material orientation noted by blue arrows.

Figure 7 Stress magnitudes and directions inside WM model in the yz-plane. Yellow arrows indicate the tensile strain direction along the global Z-direction. Under loading condition of 0.01 strain tensions in the Z-direction at the 50Hz frequency, the analysis results are shown as (a) Stress magnitudes and directions of local stress σ_{33} and (b) Stress magnitudes and directions of local maximum principal stress. The WM model material properties vary according to the different VFs and orientations in each local element. The red splines are the virtual axonal traces denoting direction and location. The arrows with different colors indicate the stress magnitudes and directions in local coordinates of each element. The unit of stress shown on the left margin is kPa.

Figure 8 Maximum principal stress magnitudes and directions of elements (a) $50\% \le VF$ and (b) 0% < VF < 50% elements (note the scales at the legends). The loading condition is 0.01 strain tensions in the Z-direction at 50Hz. The yellow cubes are elements with the VFs which are larger than 50%. The red splines signify the axonal traces. The material orientations in local z-direction are indicated by the green arrow on each element.

Table Caption

Table 1 Comparison of the orthotropic REV material properties and homogenization test results for fiber fractions (*VF*) 10%, 45% and 75%.

Table 1 Comparison of the orthotropic REV material properties and homogenization test results for fiber fractions (VF) 10%, 45% and 75%.

		Components of storage stiffness material properties tensor C'									Components of loss stiffness material properties tensor C"								
VF	(kPa)	C'_11	C'_12	C' ₁₃	C_{22}'	C_{23}'	C_{33}'	C' ₄₄	C' ₅₅	C' ₆₆	C'' ₁₁	C''_	C'' ₁₃	$\mathcal{C}_{22}^{\prime\prime}$	$\mathcal{C}_{23}^{\prime\prime}$	C'' ₃₃	C''_	C'' ₅₅	C''_66
VF	(kPa)	C'_{xxxx}	C'_{xxyy}	C'_{xxzz}	C'_{yyyy}	C'_{yyzz}	C'_{zzzz}	C'_{xyxy}	C'_{xzxz}	C'_{yzyz}	C'' _{xxxx}	$C_{\text{xxyy}}^{\prime\prime}$	C'' _{xxzz}	<i>C</i> ′′	$C_{yyzz}^{\prime\prime}$	$C_{zzzz}^{\prime\prime}$	$C_{xyxy}^{\prime\prime}$	$C_{xzxz}^{\prime\prime}$	$C_{ m yzyz}^{\prime\prime}$
10%	REV	20.0064	18.3937	18.6127	20.1447	18.6842	20.6848	0.8670	0.6959	0.6961	0.9861	0.0152	0.0006	0.9898	0.0004	1.2403	0.3244	0.2456	0.2457
	test	20.0064	18.3937	18.6127	20.1447	18.6842	20.6848	0.8670	0.6959	0.6961	0.9861	0.0152	0.0006	0.9898	0.0004	1.2403	0.3244	0.2456	0.2457
45%	REV	23.7923	22.4489	22.7665	24.3669	23.0414	25.3495	0.93341	0.3232	0.3251	1.2886	0.0420	0.0017	1.3197	0.0009	2.6168	0.4200	0.1141	0.1147
	test	23.7923	22.4489	22.7665	24.3669	23.0414	25.3495	0.93341	0.3232	0.3251	1.2887	0.0420	0.0017	1.3197	0.0009	2.6168	0.4200	0.1141	0.1147
75%	REV	44.6475	45.6190	44.4327	49.8899	47.0122	47.0970	0.9616	0.1180	0.1184	1.5116	0.0394	-0.0018	1.6678	0.0032	3.8096	0.5275	0.0417	0.0418
	test	44.6475	45.6190	44.4327	49.8899	47.0122	47.0970	0.9616	0.1180	0.1184	1.5116	0.0394	-0.0018	1.6678	0.0032	3.8096	0.5275	0.0417	0.0418

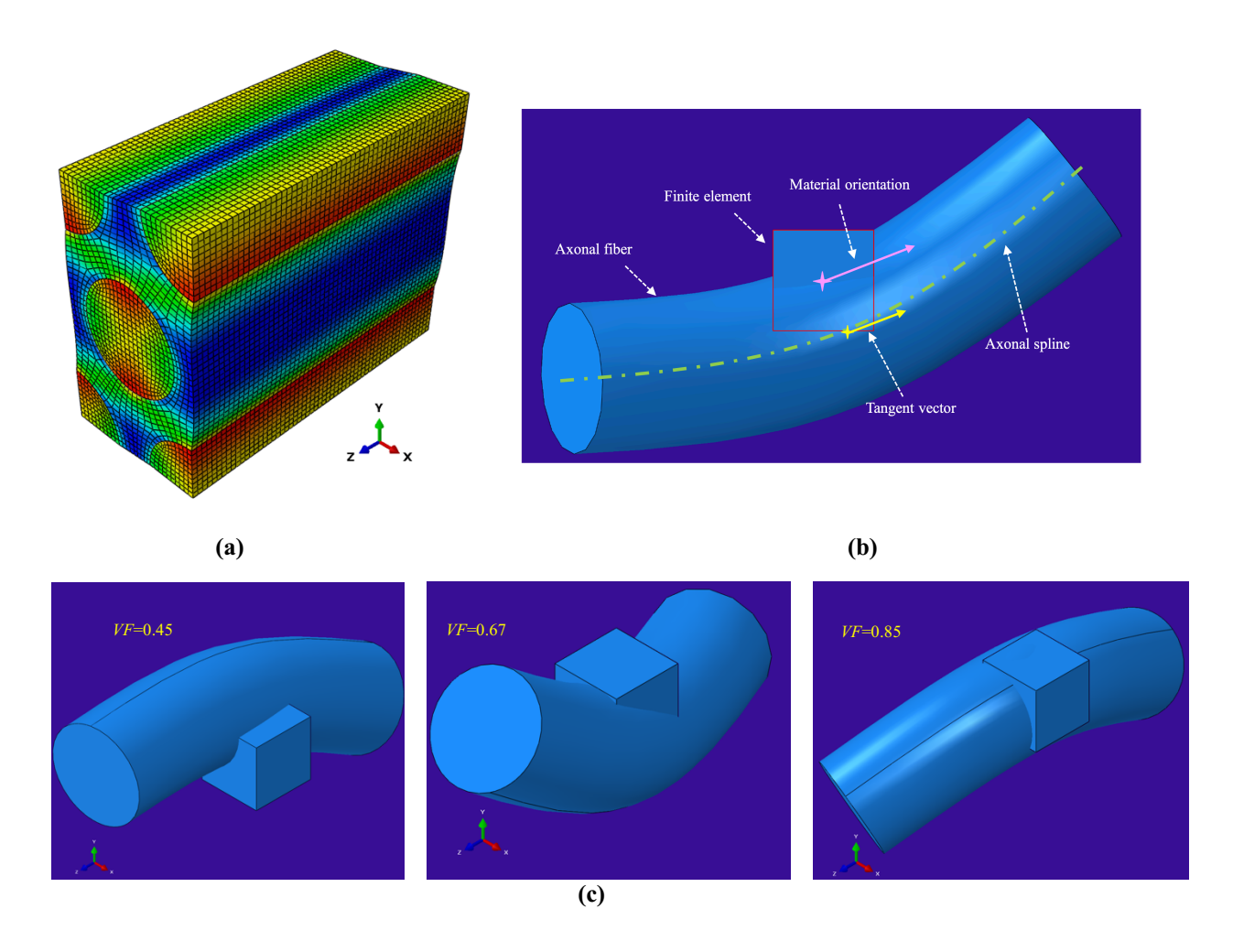


Figure 1(a) Shear stress response to XY-shear loading of a microscopic biphasic white matter REV with axonal fiber surrounded by glial phase. The axonal fibers have identical circular cross-sections and are regularly distributed in a hexagonal packing arrangement. This periodic REV allows for different packing geometries and varying mechanical interactions at the axon/glial interface. The axonal direction of REV is along the Z-direction. (b) Graphic representation of aligned orientation vectors of the finite element and axonal fiber. The pink start symbol is the centroid of this element. The pink arrow is the extracted tangent (yellow arrow) from the rebuilt axonal trace at the centroid of this element, which represents its material orientation. (c) Sample of REV training data with randomly generated *VFs* of 0.45, 0.67, and 0.85. The *VF* of this specific element will be predicted by the trained SVR model.

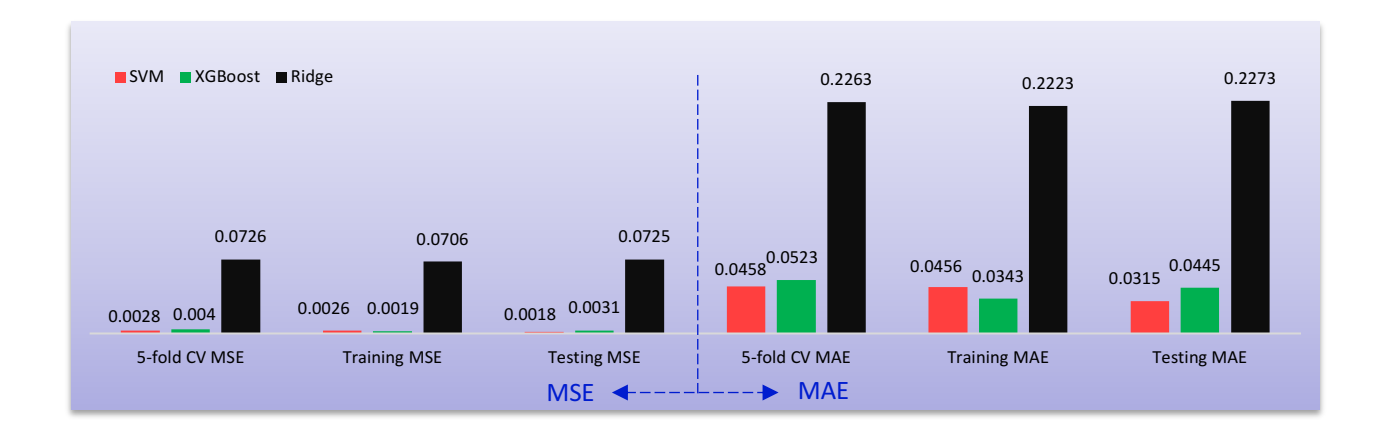


Figure 2 Graphic representation of SCV training comparison. Red bar represents SVM, green represents XGBoost used for comparing with current model, and black is Ridge regression used as baseline model. MSE (variance of residuals) and MEA (average of residuals) are used to compare the three models. SVM outperforms XGBoost and Ridge (baseline model) in both comparative sets.

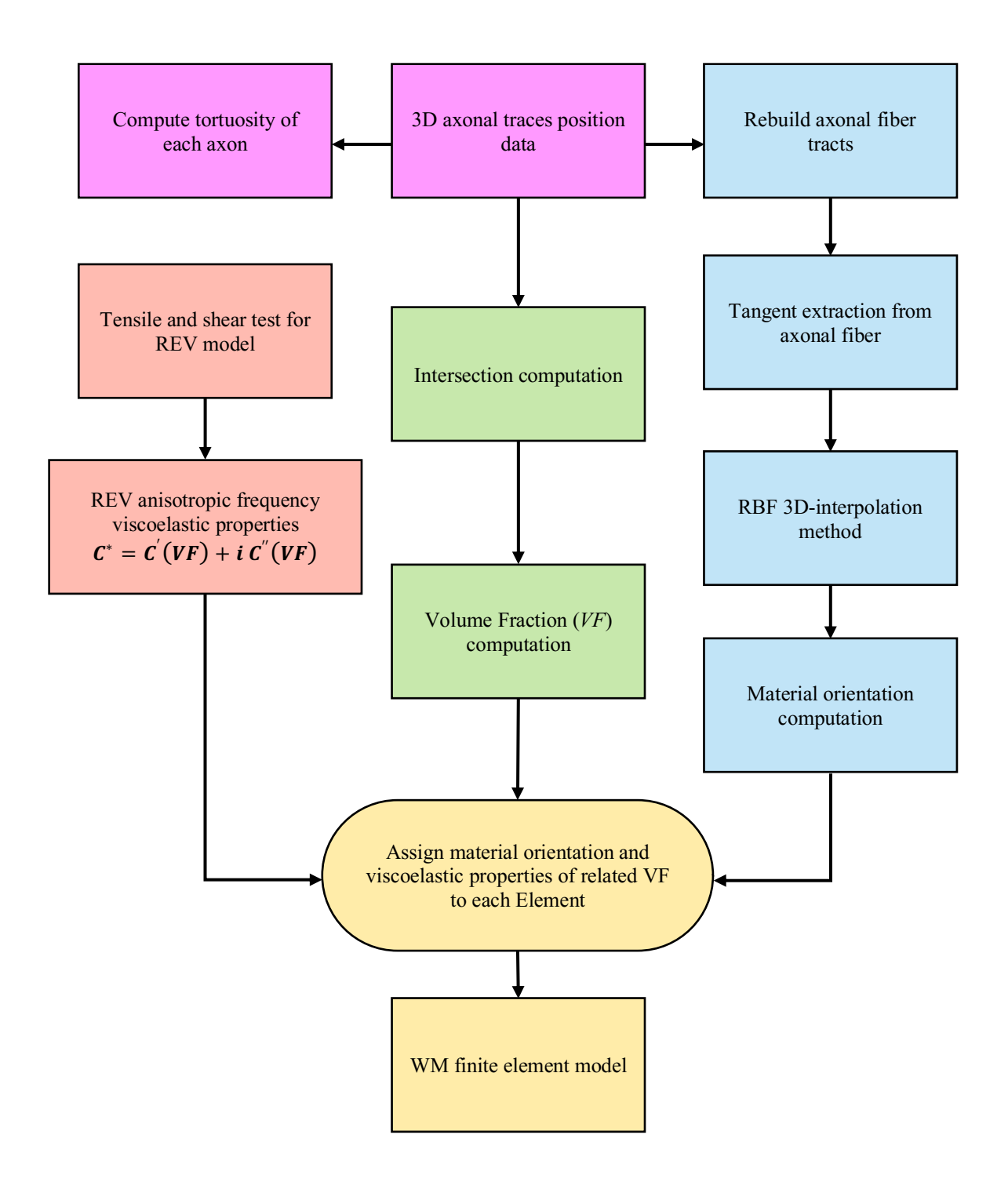


Figure 3 Algorithm for constructing the WM model using finite elements. The algorithm comprises (3) key parts: orthotropic viscoelastic material properties (salmon boxes group), V_f computed by axon position (green boxes groups) and orientation (blue boxes group) of each axon. The three parts are coupled with each other so that they can be assigned to a related element in the final WM finite element model. The pink boxes indicate the know parameters (input). The yellow boxes represent the final combination of material properties, volume fraction, and orientation for each element and the assembly of the WM FEM.

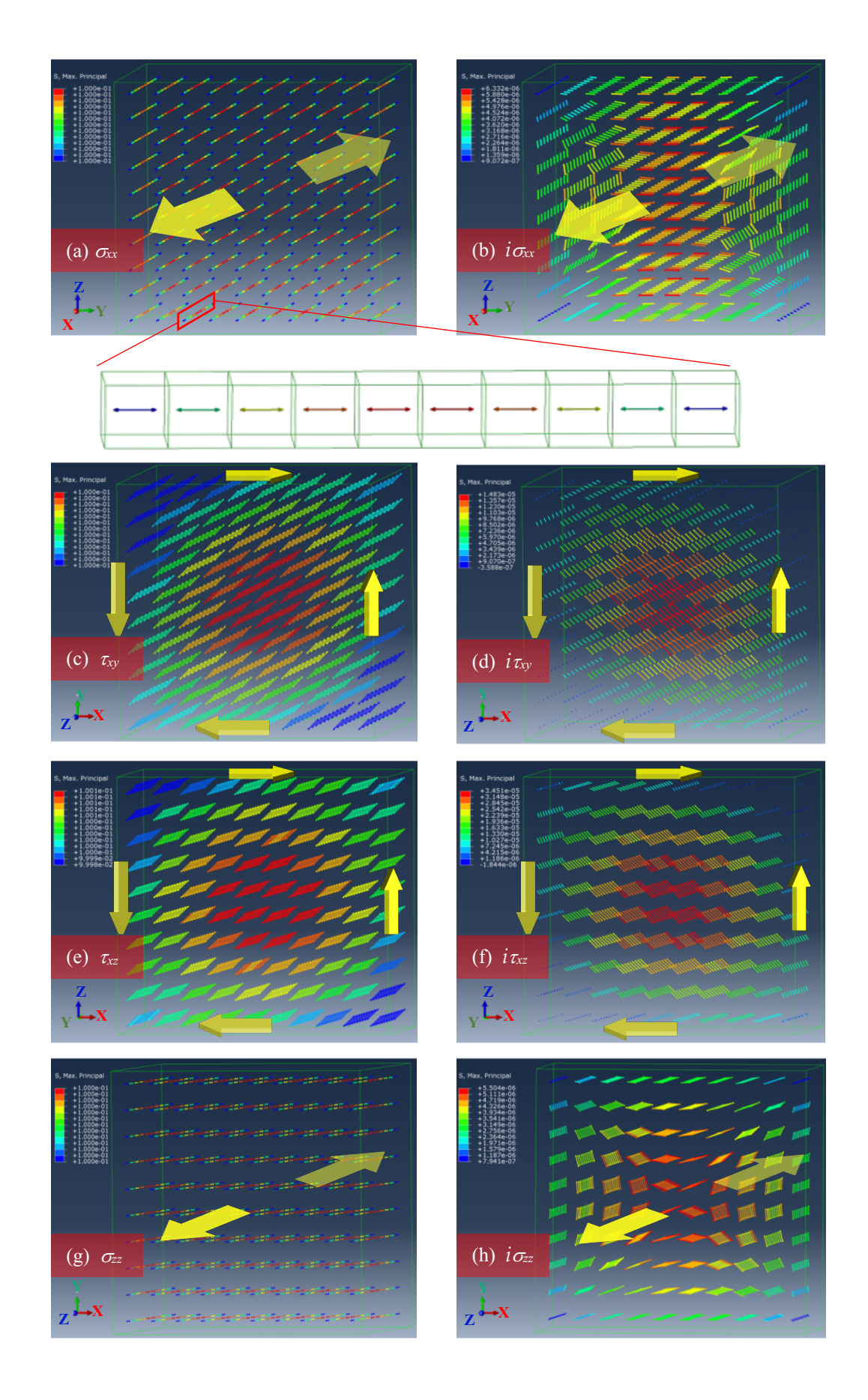


Figure 4 Representative results of maximum principal stress experienced by REV of VF = 45% subjected to 0.1 kPa in (X-, Z-, XY-, XZ-) global directions at 50 Hz frequency. The big yellow arrows indicate loading directions. The axonal direction of REV is along the global Z-direction. (a) Real components and (b) Imaginary components of maximum principal stress test in X-direction. (inset) 10 sample elements in the XX-direction from real portion result of (a). Different colors denote stress distribution. (c) Real components and (d) Imaginary components of maximum principal stress test in the XY-direction. (e) Real components and (f) Imaginary components of maximum principal stress test in the XZ-direction. (g) Real components and (h) Imaginary components of maximum principal stress test in the Z-direction. Model illustrates 10 elements in the global X-, Y-, and Z-directions amounting to 1,000 elements. The stress field at the center point of each REV is marked.

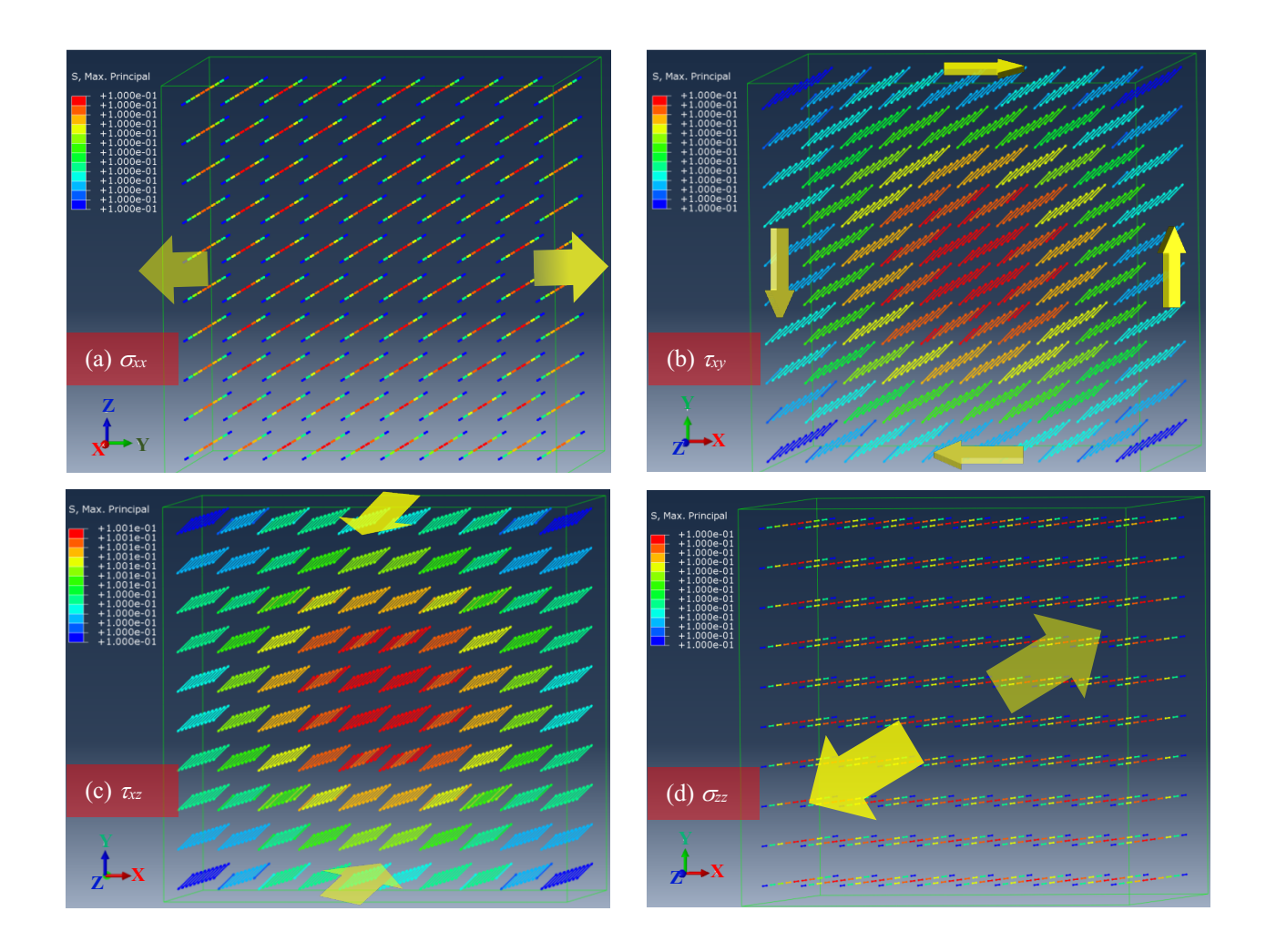


Figure 5 Dynamic amplitude results of maximum principal stress under tensile stress in (a) XX-direction, (b) XY-direction, (c) XZ direction, and (d) ZZ-direction. Dynamic amplitude is the combination magnitude of both the real and imaginary portions of the result value. Each value is the square root of the sum of the squares of the real and imaginary invariant components. The results are analogous to the real part result of each direction in Figure 4.

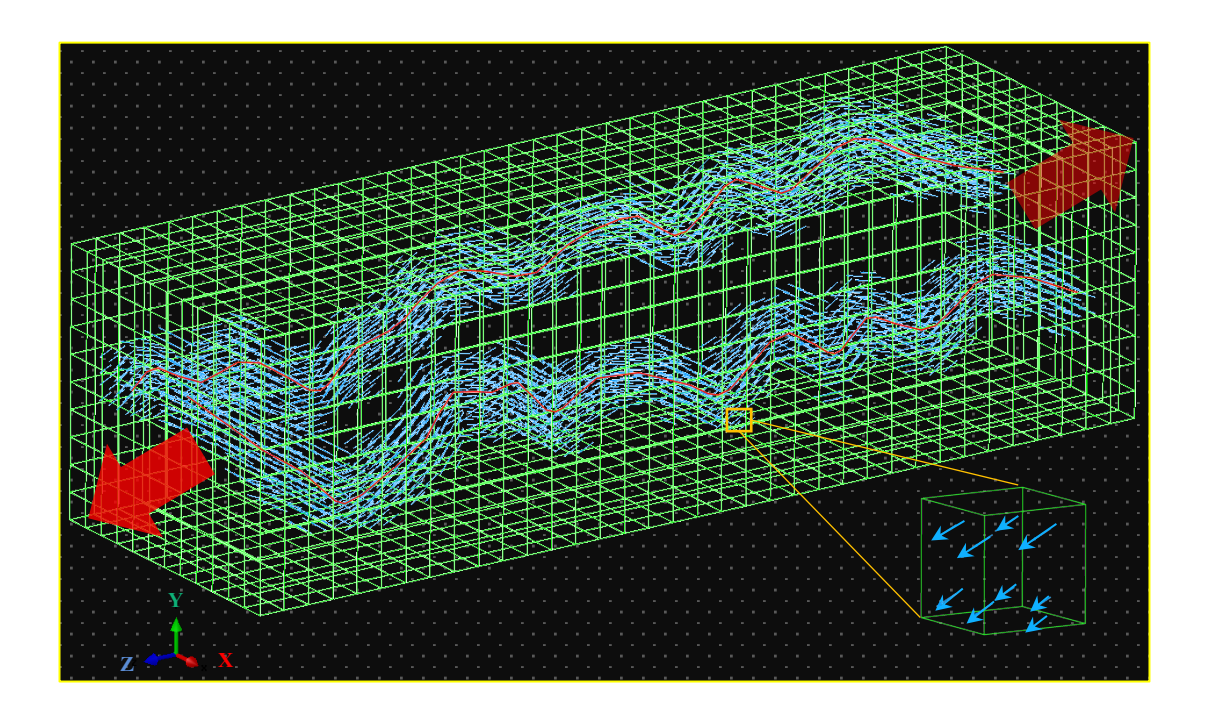
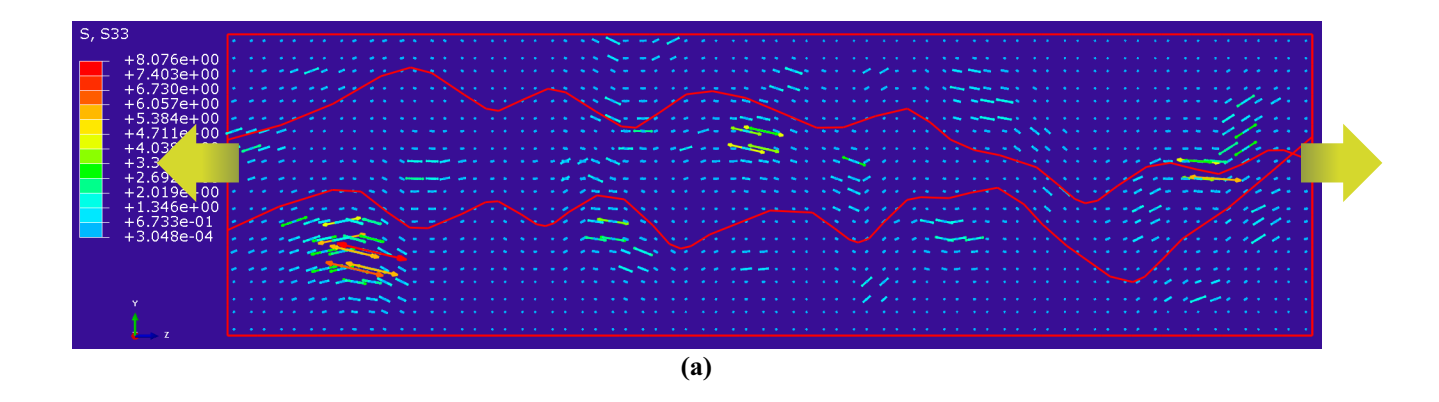


Figure 6 Mesoscopic WM model indicating axonal tract splines and material orientation in 3D space. The red splines represent the geometric axis of the axonal traces generated from axonal location coordinates data and are not included in the stress-strain analysis. There are 4,320 elements of size $20 \times 20 \times 20 \mu m$ each in the WM model. The material orientations in the z-direction of local coordinate system indicated by the blue arrows on the elements that are generated from microscopic REVs. The remaining elements without material orientation represent the pure glia phase in WM. Boundary condition is 0.01 strain tensions at 50 Hz frequency, shown as red arrows in positive and negative global Z-direction. Inset illustrates one of the elements with the material orientation noted by blue arrows.



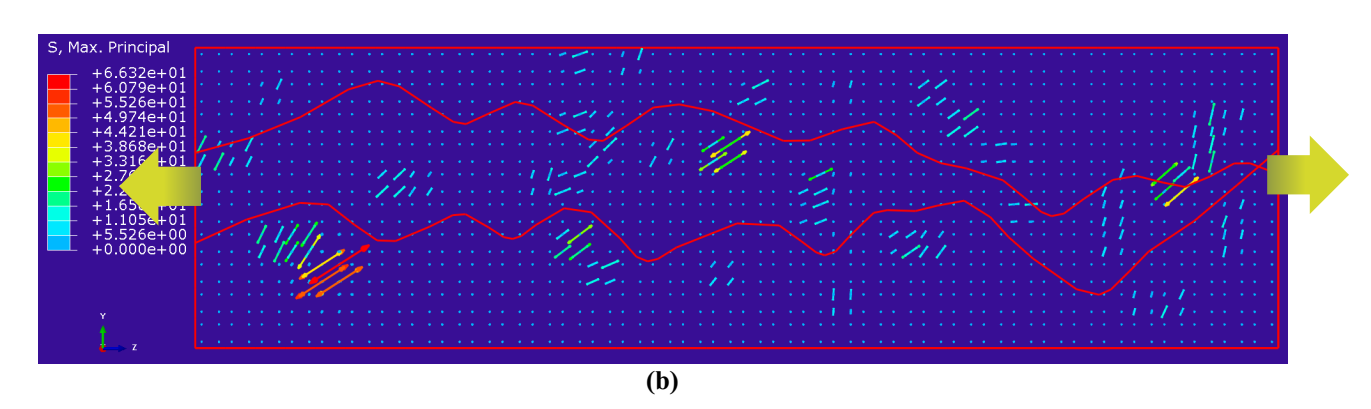


Figure 7 Stress magnitudes and directions inside WM model in the yz-plane. Yellow arrows indicate the tensile strain direction along the global Z-direction. Under loading condition of 0.01 strain tensions in the Z-direction at the 50Hz frequency, the analysis results are shown as (a) Stress magnitudes and directions of local stress σ_{33} and (b) Stress magnitudes and directions of local maximum principal stress. The WM model material properties vary according to the different VFs and orientations in each local element. The red splines are the virtual axonal traces denoting direction and location. The arrows with different colors indicate the stress magnitudes and directions in local coordinates of each element. The unit of stress shown on the left margin is kPa.

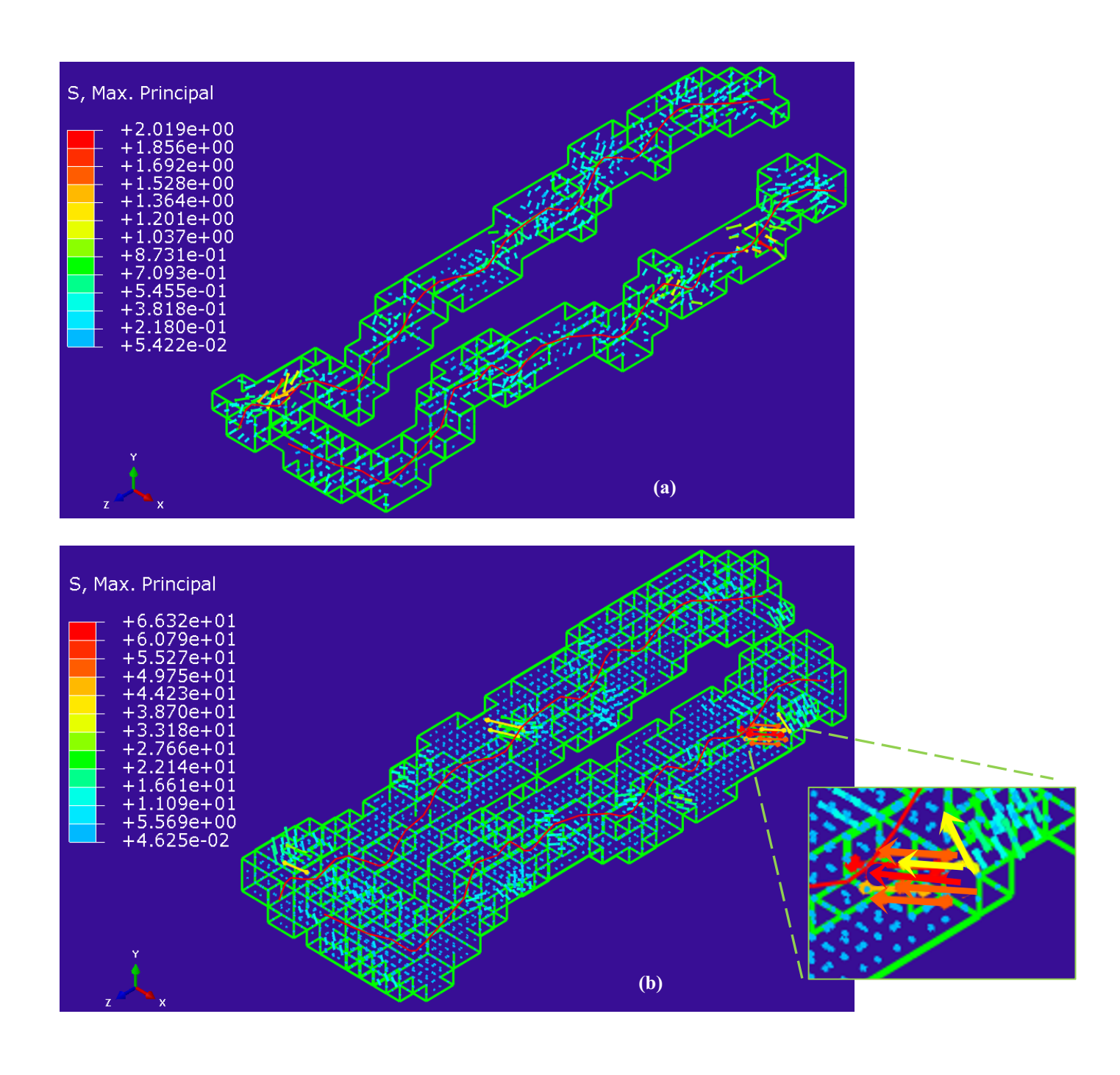


Figure 8 Maximum principal stress magnitudes and directions of elements (a) $50\% \le VF$ and (b) $0\% \le VF < 50\%$ elements (note the scales at the legends). The loading condition is 0.01 strain tensions in the Z-direction at 50Hz. The yellow cubes are elements with the VFs which are larger than 50%. The red splines signify the axonal traces. The material orientations in local z-direction are indicated by the green arrow on each element.